B0914

Infiltration of Praseodymium oxide: effect of Urea content on SOEC electrode morphologies

Clara Pioger (1,2,3), Janick Bigarré (2), Patrice Tochon (1), Jean-Marc Bassat (3)
(1) GENVIA SAS, Plaine Saint Pierre, 34500 Béziers/France;
(2) CEA, DAM, Le Ripault, F-37260 Monts/France;
(3) ICMCB-CNRS, 87 Avenue du Dr. Schweitzer, 33608 Pessac/France;
Tel.: +33-2-47-34-48-65, Mobile: +33-6-37-12-38-26
clara.pioger@genvia.com

Abstract

Reducing the operating temperatures of Solid Oxide Electrolysis Cells (SOEC) is crucial for enhancing materials durability and lowering hydrogen production costs. However, this leads to decreased kinetics, resulting in higher energy barriers for the oxygen oxidation reaction (OOR) at the anode. To address this, research is currently focusing on mixed ionic and electronic conductive materials (MIEC). Yet, state-of-the-art materials often contain alkaline-earth elements prone to diffusion and reactions within the cell and eliminating such elements from electrode compositions is therefore essential. Employing nanomaterials via surface decoration can enhance OOR as well by increasing the electrode's active surface area and improving its catalytic properties. Through the different decoration methods, infiltration is a relatively low-cost approach that can be optimized by using additives such as complexing agents to decrease particle sizes. Among these, urea shows promise for producing monodispersed nanoparticles due to its slow hydrolysis, leading to homogeneous precipitation of metal hydroxycarbonates. In this study, the effect of urea content on the morphologies of Praseodymium Oxide (PrOx) powders was investigated and PrOx powders were synthesized using six different urea-to-cation (U/C) ratios (up to 50). The impact of urea on powder morphologies was discussed and urea contents of interest for infiltration selected. Subsequently, urea-based infiltration was employed to surface decorate a conventional air electrode consisting of a $Ce_{0.9}Gd_{0.1}O_{1.95}$ (GDC) host backbone layer and a $LaNi_{0.6}Fe_{0.4}O_{3-\delta}$ (LNF) current collecting layer with praseodymium oxides. The calcinated powders were characterized using Thermogravimetric analysis (TGA), X-ray diffraction (XRD), High Temperature XRD and Infrared spectroscopy (FTIR). Further analysis involved Scanning Electron Microscopy (SEM), High-Resolution Transmission Electron Microscopy (HR-TEM), Brunauer-Emmett-Teller (BET) surface analysis, and granulometry measurements to investigate the morphologies of the oxide particles. The infiltrated electrodes were observed through cross-section Energy Dispersive Spectroscopy (EDS) to study the distribution of PrOx throughout the electrode. X-ray diffraction studies confirmed the formation of the targeted phases, with carbonate residues observed for powders synthesized at high U/C ratios (40 and 50). SEM images revealed various powder morphologies depending on the urea content. Different urea concentrations in the infiltration solution resulted in varying distributions of praseodymium within the electrode backbone. The influence of urea additives on PrOx powder morphologies and the distribution of infiltrated PrOx within the electrode will be discussed in this paper.

Introduction

According to the United Nations Office for Disaster Risk Reduction, climate change has led to a surge in natural disasters over the past decade, significantly impacting lives worldwide. Achieving the goals outlined in the 2015 Paris Agreement, limiting global warming to 1.5 °C and 2 °C, will only be possible by reaching net-zero global CO_2 emissions and making deep cuts to fossil fuel use [1]. Hydrogen emerges as a promising fuel alternative, being a carbon-free and versatile energy carrier. However, current hydrogen production methods, primarily steam methane reforming, emit carbon dioxide. Water electrolysis, producing only water as a by-product, is therefore essential for making hydrogen a sustainable and low-emission fuel. High-temperature electrolysis (HTE) offers increased efficiency compared to traditional methods, with Solid Oxide Cells (SOC) being considered one of the most efficient electrochemical devices for energy conversion However, their high operating temperature (~1000°C) accelerates the aging of the ceramic material components. Reducing the SOC operating temperatures to a range of 500°C to 700°C is therefore a significant challenge in current research in the SOC field to achieve long-term cell durability and low-cost hydrogen manufacturing. As lower resulting kinetics mean higher energy barriers needed for the oxygen evolution reaction (OER) occurring at the anode side, optimizing state-of-the-art materials and discovering highly efficient novel materials for the cell components is imperative to boost the cell performance. [2] The oxygen electrode significantly contributes to the cell polarization resistance and current research is thus focusing on mixed ionic and electronic conducting materials (MIECs) with high oxygen ion diffusion and surface exchange coefficients. These materials increase the oxygen surface exchange kinetics by delocalizing the active sites for the oxygen evolution reaction (OER) along the triple phase boundaries (TPBs) on the entire surface of the electrode as well as the oxygen ions bulk diffusion [2]. However, state-of-the-art MIEC materials often contain alkaline-earth (Sr) and transition (Co) elements that readily diffuse and/or react with other components of the cell. Therefore, research aims to exclude such elements from the chemical composition of the electrode. Recently, Pr_6O_{11} has gained significant interest due to its very high electrocatalytic activity at intermediate temperatures. It exhibits exceptional oxygen diffusion and surface exchange coefficients of 3.4×10^{-8} $cm^2.s^{-1}$ and 5.4×10^{-7} $cm.s^{-1}$ at 600 °C [3], making it an excellent electrocatalytic material for the oxygen reduction reaction (ORR). Moreover, it demonstrates mixed ionic and electronic conductivity thanks to the Pr^{+III}/Pr^{+IV} mixed valency and a well-distributed oxygen vacancy in its fluorite cubic structure [3]. Despite its low electrical conductivity, of $\sigma_e < 4$ $S.cm^{-1}$ for the operating temperature of interest [4], its electrochemical activity remains high when used as an oxygen electrode, with a polarization resistance of only 0.026 $\Omega.cm^{-2}$ at 600 °C [3]. However, it's worth noting that Pr_6O_{11} easily changes into Pr_9O_{16}, Pr_7O_{12}, and/or Pr_2O_3 depending on the temperature and mainly surrounding pO_2 [5]. These phase transitions induce dimensional variations, leading to significant mechanical stress within the material, which limits its use as a single electrode material when produced using the common screen-printing method. Surface decoration of a MIEC oxide on an oxygen conducting backbone allows obtaining a high specific surface area and the creation of interconnected network of nanoparticles, thereby enhancing catalytic activity through an extended triple phase boundary (TPB) length of the oxygen electrode [6]. Such so-called infiltration method is a relatively low-cost and easy approach widely used in the surface modification of SOC electrodes. It involves carrying soluble metal salts in a solution prior to the infiltration step. At this first stage the use of additives such as surfactants, precipitating, or complexing agents is often employed to decrease the particle sizes. Among these additives, urea is particularly promising for obtaining monodispersed nanoparticles. Its slow hydrolysis releases anionic species into the aqueous solution,

regulating the crystallization behavior and thus resulting in the homogeneous precipitation of metal hydroxycarbonates [7].

1. Scientific Approach

To further investigate the effect of urea content on the morphologies of PrOx powders, these ones were synthesized using six different urea concentrations. The impact of the urea additive on the oxide powder morphologies and phase structures was discussed and different urea concentrations of interest in the infiltration solution were thus selected. Herein, urea-based infiltration was employed to surface decorate a conventional air electrode, composed of a host backbone layer $Ce_{0.9}Gd_{0.1}O_{1.95}$ (GDC), and a current collecting layer, $LaNi_{0.6}Fe_{0.4}O_{3-\delta}$ (LNF), with nano-particles of praseodymium oxides.

2. Experimental Methods

2.1. Samples preparation

- Powder synthesis

Praseodymium oxide (PrOx) powders were synthesized using a nitrate combustion method. Initially, starting materials $Pr(NO_3)_3.6H_2O$ were dissolved in a solvent mixture of reverse osmosis water/ethanol. Urea was then added as a complexing agent, and the molar ratios of praseodymium cation to urea were varied at 0, 10, 20, 30, 40, and 50. The solution was stirred and heated up to 100 °C until a homogeneous gel is formed. Subsequently, the gel was heated at 200 °C to obtain dried precursors. These ones were then calcined at 600 °C for few hours under a static air atmosphere to produce the PrOx powders, labelled as U0, U10, U20, U30, U40, and U50, respectively.

- Infiltration

The GDC backbone layer and the current collecting layer LNF were successively screen-printed onto a dense 8YSZ electrolyte support. The bi-layer structure was co-sintered under a static air atmosphere to ensure a good mechanical resistance of the porous supported backbones. To prepare the urea-based infiltration solution, $Pr(NO_3)_3.6H_2O$ was dissolved in a solvent mixture of reverse osmosis water and ethanol) with different molar ratios of Urea to Pr cations of 0, 10, and 20. The solutions were stirred at room temperature until complete dissolution of the materials. The backbones were impregnated with the infiltration solution and excess nitrate solution was removed with absorbent paper, and the wetted backbones were subjected to primary vacuum to distribute the solution throughout the thickness of the backbone. Subsequently, the impregnated backbones were fired at about 500 °C for 20 minutes to form the oxide phases and remove the nitrates and urea residues. These steps were repeated until the targeted loading of PrOx was achieved. The infiltrated electrodes are referred as inf-U0, inf-U10, and inf-U20 for simplicity.

2.2. Materials characterization

- Phase and crystallographic structure

The Fourier Transform Infrared (FTIR) spectra recorded on the PrOx powders were recorded using a Nicolet iS50 spectrophotometer to investigate the nature of bonding, the

presence of nitrate residues and the potential intermediate products formed with urea. The measurements were performed using an Attenuated Total Reflectance (ATR) set up in a range of 2000 to 400 cm^{-1}. X-ray diffraction (XRD) analysis was performed to study the composition and crystallographic structure of the obtained PrOx at room temperature. The diffractograms were collected in the 2θ range of 10-90 ° using a PANalytical X'pert MPD diffractometer (Malvern Panalytical, United Kingdom) with Cu-K_α incident radiation ($\lambda K_{\alpha1}$ = 1.5406 Å and $\lambda K_{\alpha2}$ = 1.5444 Å). Phase analysis was performed using DIFFRAC.EVA software (Bruker, United States). Powders U0, U10, U20, and U50 were characterized *in situ* using high-temperature XRD with a PANalytical X'pert equipped with an HTK1200 chamber and a Co-Kα incident radiation source to investigate the phase transitions under an air flow atmosphere. The diffractograms were collected during the heating process at 25 °C, 200 °C, and then after each 100 °C increment until 1100 °C using a heating rate of 2 $°C.min^{-1}$. After heating, the samples were cooled to 25 °C at a cooling rate of 10 $°C.min^{-1}$ to study the reversibility of the phase transition process. A dwell time of 1 hour was set up at each temperature to equilibrate the powder before starting the X-ray analysis. The thermal behavior of the powders U0, U10, U20, and U50 was studied through Thermogravimetric Analysis (TGA) using a TA-Instrument Q500 device. Materials were heated under an airflow of 60 $mL.min^{-1}$ up to 1000 °C, then cooled down to room temperature at a rate of 2 $°C.min^{-1}$.

- Morphologies

The microstructure of the powder samples was observed *via* scanning electron microscopy (SEM) using a JSM-IT200 (JEOL, Japan). The powder was ground in a mortar and deposited on a carbon film tape. Polished cross-sections of the electrodes with and without infiltrated PrOx were studied through energy dispersive spectroscopy (EDS) (Bruker, United States) cartography to observe the distribution of the praseodymium element within the electrode and thus the infiltration homogeneity. High-resolution SEM (HR-SEM) images were obtained for cross-sections of electrodes with and without infiltrated PrOx using a JEM 6700F FEG microscope (JEOL, Japan). The samples inf-X were fractured to observe the morphology of the infiltrated particles more precisely. All samples studied with SEM were coated with a thin sputtered platinum film (< 5nm) to avoid electron charging. Granulometry measurements were conducted using a Mastersizer 2000 laser granulometer (Malvern, United Kingdom) with a wavelength of 633 nm. The nitrogen adsorption/desorption isotherms were performed using a Micromeritics Gemini apparatus. 0.5 g of the powder samples were priorly dried 1 hour at 90 °C then 12h at 300 °C. High-Resolution Transmission Electron Microscopy (HR-TEM) measurements were performed using a JEOL JEM 2200FS apparatus to examine the morphologies of the powders particles. The specific surface area of the synthesized samples was measured using the Brunauer, Emmett, & Teller (BET) method. Additionally, Barrett-Joyner-Halenda (BJH) models were applied to calculate the volume of meso-to-macropores from the isotherm data.

3. Results

Different colors of PrOx powders were obtained, starting from a black/dark brown color, which brightened with increasing urea content until a brown color was achieved. Three hypotheses for this color difference are proposed:

1. Different oxide stoichiometries were obtained with different bandgap energies.

2. An important difference in the morphologies of the powders could change its refraction, affecting the way it reflects light.
3. Intermediate products formed with urea could have remained due to inefficient calcination (low temperature or short calcination time).

- Phase and crystallographic structure

The Fourier-transform infrared spectra of all powder samples are depicted in Fig. 1. A medium peak at 1370 cm^{-1} is observed in all samples, which intensity begins to decrease after U40. This is likely attributed to the Pr-O stretching band, as observed in this frequency range for other rare earth oxides [7]. Additionally, another band is also evidenced for all samples at 590 cm^{-1} [7]. The adsorption peak at 1470 cm^{-1}, also seen for all powders and becoming sharper starting from U40, suggests the powders contain remaining carbonates, which amount increases with the urea content [7]. It should be noted that this adsorption peak could also be attributed to the C-N stretching frequency, as another peak, observed starting from U40 at 1500 cm^{-1}, could be assigned to the N-O stretching vibration [8]. Therefore, persistent nitrate residues could remain. Furthermore, both the elongation of the C-O band and the symmetrical stretching of NO_2 could be associated to the peak seen at 1090 cm^{-1} starting from U30 and upper compositions. A minor peak, present in all samples but becoming sharper and more prominent starting from U40 and upper compositions, is observed at 850 cm^{-1}, that could be assigned to the deformation of C-H or the bands of NO_2 out-of-plane rocking. However, considering that nitrates are decomposed around 350 °C, these assumptions seem unlikely.
From these FTIR spectra, we conclude that all powder samples contain carbonate contents, with higher concentrations starting from U30 and the more urea-rich compositions. The resolution of the FTIR measurements is insufficient to observe differences in Pr-O vibration frequency shifting, which could indicate variations in the nature of the Pr band and therefore the valency state of Pr.

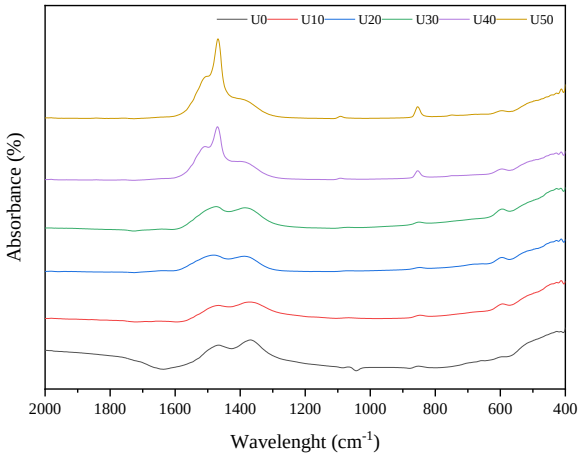

Fig.1. FTIR spectra recorded on PrOx powders calcinated at 600C °C with different urea contents.

X-ray diffraction patterns recorded on the as-synthesized powders of praseodymium oxides calcinated at 600 °C are plotted in Fig. 2. The targeted Pr_6O_{11} (⇔ $PrO_{1.83}$) phase was obtained for all samples. A double phase of Pr_6O_{11} and PrO_2 was obtained for the pristine sample U20, with a residual peak of Pr_4O_7 (⇔ $PrO_{1.75}$) where Pr is completely oxidized to the valency state of IV^+ [5]. Therefore, this phase possesses a non-mixed valency, which is undesirable for achieving good oxygen transport properties. However, peaks associated

with this phase tend to disappear starting from U10. Carbonate residues of $Pr_2O_2CO_3$ were found starting from U40.

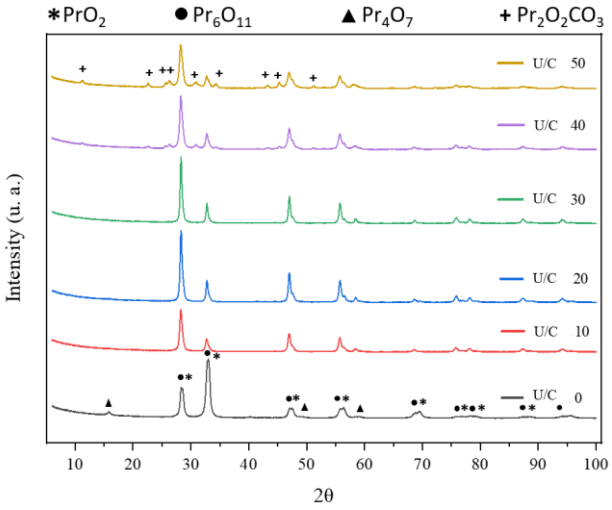

Fig.2. XRD powder diffractograms obtained for calcinated products (600°C) of urea mixed with praseodymium nitrates with a urea-to-cation ratio of 0, 10, 20, 30, 40, and 50 .

To obtain information on the temperature of decomposition of the carbonate residues, *in situ* HT-XRD was performed on sample U50. The X-ray diffraction patterns obtained upon heating up to 1100 °C under an air flow atmosphere are shown in Fig. 3. The $Pr_2O_2CO_3$ phase was removed at 900 °C, indicating that an *in situ* removal of a working SOC cell would not be possible, as the targeted operating temperature range is between 500 and 800 °C. Morever, from 25 °C to 1000 °C, a slight shift of the main peak initially located at 28.0° 2θ was observed, this value increasing to 28.4 °2θ at 1000 °C, then decreasing to 27.6 °2θ at 1100 °C. This indicates that the lattice parameter 'a' is decreasing until 1000°C and then increases again at 1100 °C. The intensity of this peak is also significantly reduced for the diffraction patterns acquired at both 900 °C and 1000 °C, suggesting a phase transition occurring from 1000 °C to 1100 °C. However, the value of the cell parameter is again stabilized to 28.05 °2θ upon cooling to room temperature. A conclusion is that the Pr_6O_{11} phase (1/3 Pr^{3+} and 2/3 Pr^{4+}) is stable at low temperatures only; it loses oxygen as the temperature increases, thus together with a partial reduction of Pr^{4+} ion to Pr^{3+} and also undergoes several phase transitions.

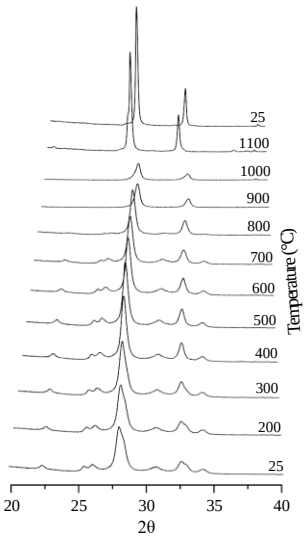

Fig. 3. *In situ* High-Temperature powder diffractograms of U50 recorded under air up to 1100 °C

Thermogravimetric analysis (TGA) experiments were performed to study the weight losses heating to 1000 °C and cooling to room temperature under an air flow atmosphere. As seen in Fig. 4., upon heating, three weight losses were observed for samples U0, U10, and U20 at approximately common temperatures, with an additional loss only found for sample U50. A first phase transition around 290°C is observed for all samples and is even more evident for U0; this sample containing a double phase of PrO_2 and Pr_6O_{11}, the observed phenomenon could correspond to the phase transition of the remaining PrO_2 into Pr_6O_{11}. Then, as the temperature rises above 400 °C the anionic order of Pr_6O_{11} is lost, and the phase is slowly reduced with partial reduction to Pr_7O_{12} observed around 710 – 730 °C [4]. No weight loss is observed from 750°C to 930°C, indicating that Pr_7O_{12} is more stable at higher temperature. This is in good agreement with the literature as Pr_7O_{12} possesses ordered oxygen and does not lose oxygen until 1000 °C [4]. However, a final weight loss occurring around 930-940 °C is observed, which could correspond to the total reduction towards fully reduced Pr_2O_3 ($\Leftrightarrow PrO_{1.5}$). As multiple stoichiometries of PrOx exist, these assumptions have to be carefully considered. In our opinion the supplementary weight loss observed around 580 °C for sample U50 resulted from the decomposition of remaining carbonates (as carbonate residues persisted during *in-situ* HT XRD until 900 °C). All three samples show similar thermal behaviour upon cooling back to room temperature, with two weight gains occurring: a first one located at 930 °C for U0 and around 845 °C for U10 and U20, and then secondly at 650°C for all three samples. Stable plateaus are observed, corresponding to two stable orders of oxygen vacancies. However, no gain loss and thus no oxidation is observed from 700 °C to room temperature, evidencing an incomplete re-oxidation of the samples under air flow atmosphere.

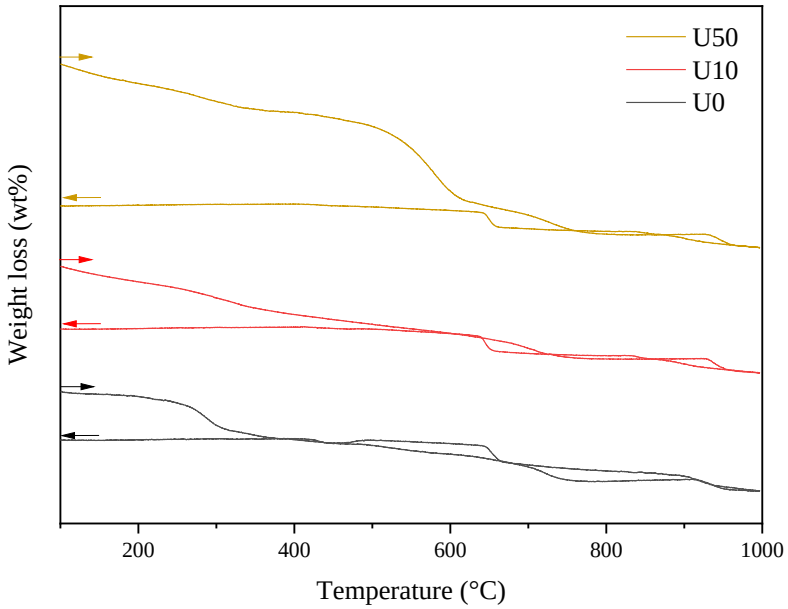

Fig.4. TGA curves recorded on U0, U10 and U50 under air flow atmosphere

- Morphologies

Different morphologies of PrOx powders as a function of the urea content were observed by SEM. SEM images are shown in Fig. 5. For U0, crystal plaquettes with highly heterogeneous sizes and shapes were observed. For U50, large agglomerates of powder particles were observed, indicating a considerable reduction in particle size at this urea-to-citrate (U/C)

ratio, as well as more uniform particle shapes. Therefore, urea successfully allowed the obtention of uniform powder particles.

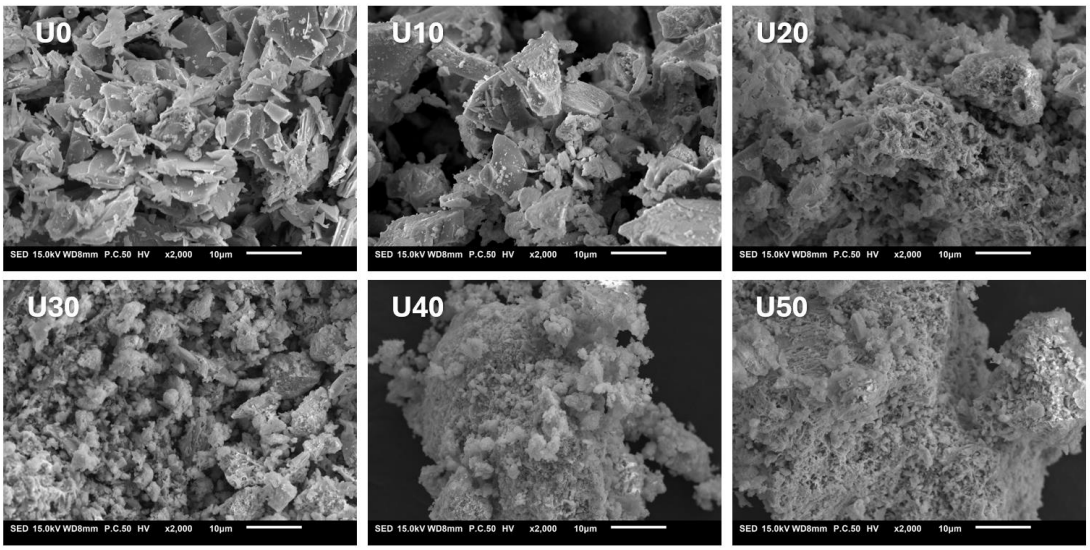

Fig. 5. SEM images recorded on PrOx obtained from different urea content.

Granulometry measurements were performed in liquid dispersion to analyse and compare the particle size distribution in the different powder samples. The parameters obtained from granulometry include d_{10} and d_{50}, which represent the particle size below which 10% and 50% of the particles fall, respectively, and the data are represented in Fig. 6. To address the agglomeration and ensure accurate results, measurements were conducted with and without prior ultrasound treatment applied to the sample solution before the measurements. The d_{10} values tend to diminish as the urea content increases, with a reduction in d_{10} of almost 20% with U50. The d_{50}, which is more associated with the agglomerate behaviour of the powder, diminishes by 45% with U50. However, a small increase in d_{10} and a significant increase in d_{50} are observed for U20 and U30. This could be explained by the diminishing particle size and thus the increasing surface activity and reactivity of the particles, resulting in a stronger agglomeration behaviour that is harder to disaggregate using ultrasounds. As no residues of praseodymium carbonates were seen for U20 and U30, their associated urea content are therefore optimal for both structural and morphologies properties.

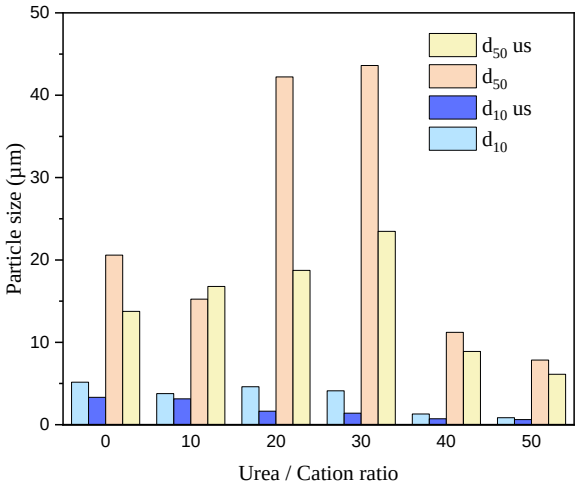

Fig.6. Distribution of particle size in powder samples synthetized with different urea cation contents (in volume)

During isotherm measurements, dried samples were exposed to N_2, and the amounts of adsorbed gas were measured in the relative pressure (p/p_0) range of 0.000–0.993, where p is the actual gas pressure during the experiment, and p_0 is the saturated vapor pressure of N_2 under laboratory conditions. Specific surface areas (S_{BET}) were obtained from the nitrogen adsorption and desorption isotherms and the data are reported in Table 1.

U/C	0	10	20	50
S_{BET} ($m^2.g^{-1}$)	24,2	13,9	15,2	23,9

Tab.1. Evolution of the Specific Surface Area, density and particles sizes values as a function of the molar U/C ratio

.

S_{BET} of the pristine sample U0 is 24.2 $m^2.g^{-1}$ and is seen to almost halve with U10, contradicting the granulometry results. However, S_{BET} value increases to 23.9 $m^2.g^{-1}$ for U50. The lower S_{BET} values measured on U10 and U20 could result from the agglomeration of the powder samples. This was confirmed using the Barrett, Joyner, and Halenda (BJH) method (see Fig.7.), which uses the Kelvin equation to convert the equilibrium adsorption data into pore size distributions. This method provides informations on the distribution of the pore sizes and volumes within the material. It can distinguish between micro, meso, and macroporosities. The pore size distribution showed mesoporosity (2 nm < pore diameter < 50 nm) for all materials, with an increase in pore diameter observed as urea content rises. As no porosity was observed *via* SEM for all powders, the mesoporosity could be associated with the inter-particularity of aggregates. Macroporosity (> 50 nm) is observed in U20 and U50 powders and could be associated with external surface and thus inter-particularity. However, U50 showed higher S_{BET} and pore volume than U20 and could also have a greater internal surface. As these oxide powders exhibit complex porosity, caution is advised in the interpretation of these results. Nevertheless, the increase in the inter-particulate porosity with urea content is consistent with the SEM observations and granulometry measurements, suggesting that powder aggregation increases with urea content. The stronger aggregate behaviour could be explained by the reduction in particle size of PrOx powders, leading to an extended surface area and its increased reactivity. This suggests that the particle sizes diminish with increasing urea content.

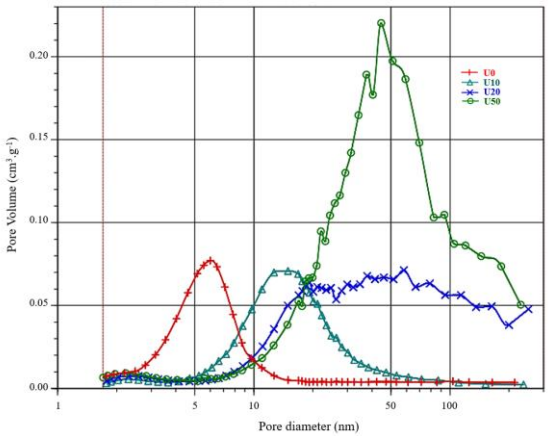

Fig.7. Pore size distribution calculated from BJH method.

An analysis of the morphology and particle size of the PrOx nanoparticles was also performed by HR-TEM analysis. Fig. 8. shows micrographs of U0, U10, and U50. In the case of U0, particles exhibit highly heterogeneous size with variable shapes. U10 shows a

very homogeneous distribution of smaller spherical crystallites. Due to the tendency to form aggregates, it is challenging to evaluate the particle size for both U10 and U50. However, larger crystallites with a more heterogeneous distribution of sizes seem to appear for U50. This could be attributed to the presence of both PrOx and praseodymium carbonates.

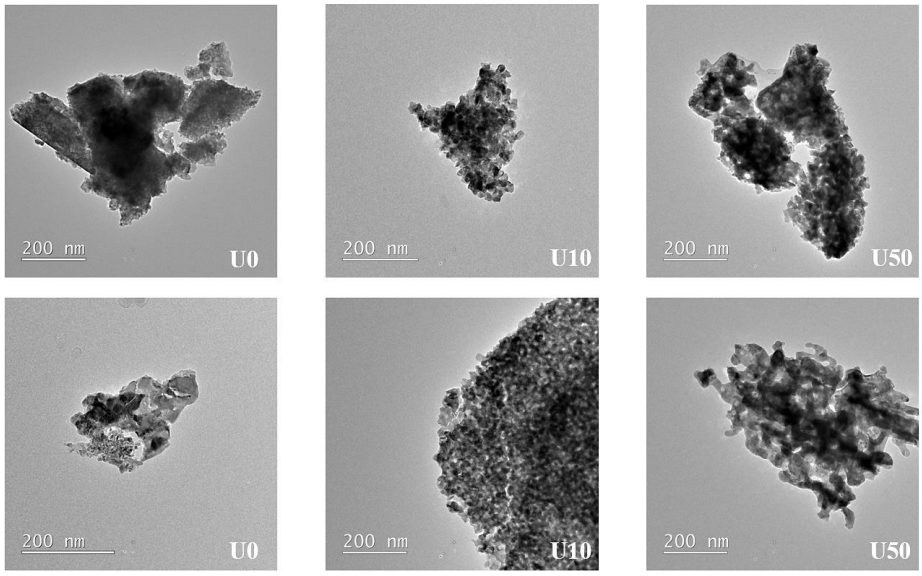

Fig.8. HR-TEM images of U0, U10 and U50.

As the agglomeration tendency of the powders makes the particle characterization challenging, the particles infiltrated and bonded to the backbone were also observed. Two locations in the backbone were investigated through HR-SEM: the middle of the thickness of the LNF layer and near the electrolyte region insides the GDC layer. Inf-U0, seen in Fig. 9.b, shows uneven distribution through the LNF grains with flat aggregates of PrOx that seem to agglomerate into horizontal blocks. In Fig. 9.c, inf-U10 shows smaller PrOx agglomerates with a greater variety of agglomerate shapes, while inf-U20 shows a very thin coverage of the LNF grain, with fewer and small agglomerations at some LNF grain edges on Fig. 9.d. EDX analysis is necessary to confirm the presence of PrOx here; however, inf-U20 possess smoother grain boundaries and surface when compared to the non-infiltrated skeleton (Fig. 9.a), thus suggesting a coverage of the grains. GDC layer shows smaller grains and less porosity compared to the LNF layer and when infiltrated, large blocks of PrOx agglomerates are observed again for inf-U0, with some parts of the GDC grains left uncovered. As the urea content increases, the infiltrated GDC region observed appears denser and more compact, with the porosity filled. This is undesired, as the gas phase space is reduced, and TPB active sites are reduced as well.

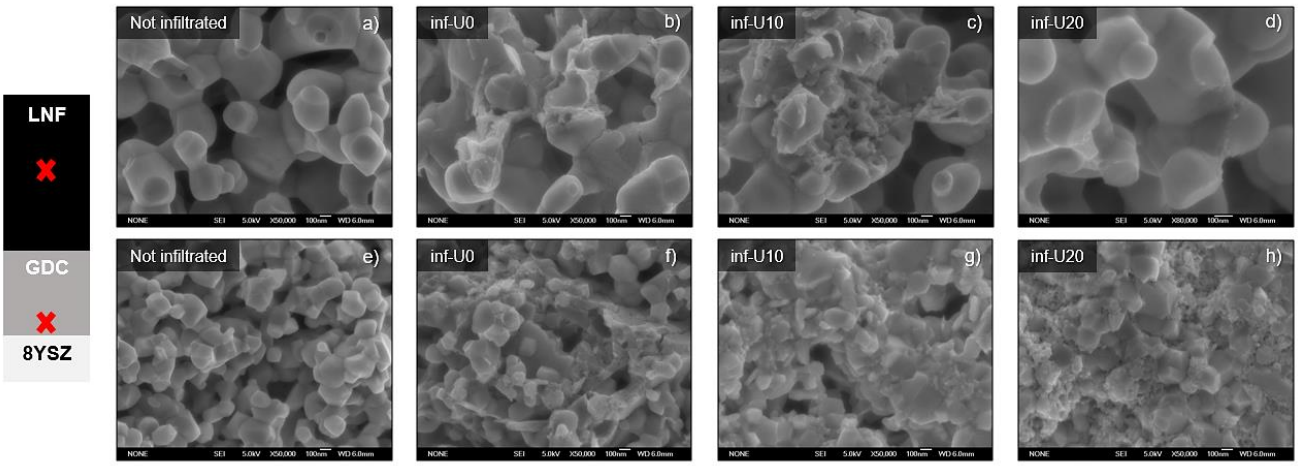

Fig. 9. HR-SEM images recorded on cross section of infiltrated backbone using different urea contents in the infiltration solution, in both the LNF (a-d) and in GDC regions (e-h).

EDS maps of the praseodymium element in polish cross-sections of infiltrated backbones are shown in Fig. 10. Infiltration was successful for all samples, and different distributions of praseodymium are observed. As the photon emission energies of the $L\beta_1$ lines of lanthanum and the $L\alpha_2$ lines of praseodymium are very close, making their separation and distinction in EDS impossible, a highlight of Pr element in the LNF layer does not necessarily indicates a higher concentration of praseodymium. Homogeneous distributions of Pr throughout the overall thickness of the GDC skeleton are observed for inf-U0 and inf-10. However, it is difficult to determine whether the increased brightness in inf-10 is due to a higher amount of PrOx or a thinner distribution. Weight measurements of PrOx can be imprecise, but the three skeletons were infiltrated with approximately the same amount of PrOx. Regarding inf-U20, EDS Map is in good agreement with the HR-SEM images whereas praseodymium appears to be more localized near the electrolyte region.

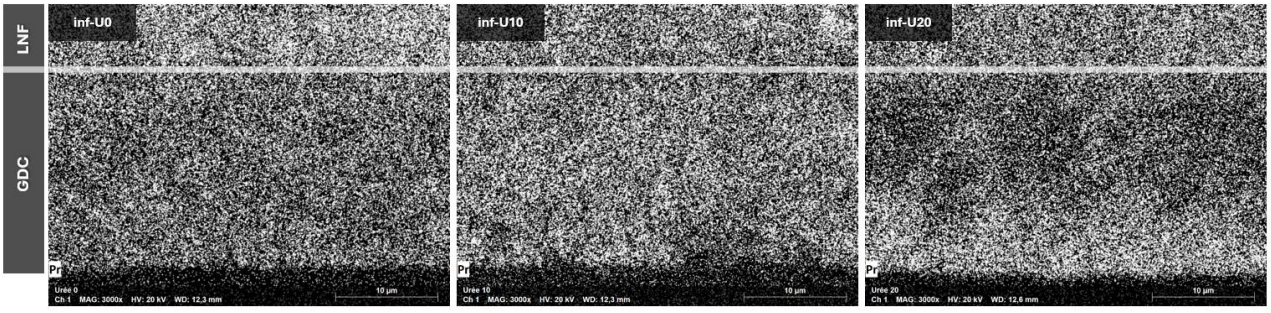

Fig. 10. EDS Mapping of the praseodymium distribution in cross sections of the electrode using different urea contents during infiltration.

Conclusion

The thermal behavior and phase transitions were investigated on Praseodymium oxide powders obtained through different urea contents. U10 and U20 leaded to obtain the targeted phase of PrOx, whereas a double phase with insulating PrO_2 was observed for the pristine sample. *In situ* HT-XRD revealed the removal of carbonate residues at 900 °C, indicating that U/C ratios equal or above to 30 are unpromising for infiltration purpose.

The increase in the urea content also led to higher inter-particulate porosity of the powders, indicating an increased aggregation. This stronger aggregate behavior is likely due to the reduction in particle size of the PrOx powders, resulting in an increased surface area and reactivity. Successful infiltration of Praseodymium oxide (PrOx) into the electrodes was achieved for all infiltrated samples. EDS mapping revealed different distributions of praseodymium throughout the backbone: while inf-U0 and inf-U10 exhibited homogeneous distributions of praseodymium throughout the GDC layer; the rare-earth was more localized near the electrolyte region for inf-U20, also confirmed by HR-SEM observations. As urea content increases, the infiltrated GDC region becomes denser and more compact, reducing gas phase space and TPB active sites. Consequently, poorer electrochemical performances are expected for inf-U20. However, it should be noted that after changing the morphologies of the infiltrated material, the variation of its weight loading content into the backbone must be reconsidered in the aim of achieving thinner coverage of backbone without significantly reducing the electrode porosity. The characterization of the electrochemical performances of inf-10 by Electrochemical Impedance Spectroscopy (EIS) is necessary to provide insight into the study perspectives and further studies should explore lower infiltration rates for U10 and U20 as well as intermediate U/C content such as inf-U15.

Acknowledgments

This work was supported by the french National Agency of Research and Technology (ANRT). The authors would like to thank Marie Anne Dourges and Guillaume Clermont (ISM, Bordeaux) for nitrogen adsorption and desorption measurements, Jingxian Wang (PLACAMAT-CNRS) for HR-TEM analysis, Sonia Buffière (ICMCB) for HR-SEM images, and Laetitia Etienne (ICMCB) for granulometry measurements.

References

[1] Kakoulaki G., Kougias I., Taylor N., Dolci F., Moya J., Jäger-Waldau A. (2021). Green hydrogen in Europe - A regional assessment: Substituting existing production with electrolysis powered by renewables. Energy Conversion and Management, 228,113649.
https://doi.org/10.1016/j.enconman.2020.113649

[2] Laguna-Bercero M.A., Kilner J.A., Skinner S.J. (2010). Performance and Characterization of (La,Sr)MnO3/YSZ and La0.6Sr0.4Co0.2Fe0.8O3 Electrodes for Solid Oxide Electrolysis Cells. Chemistry of Materials, 22 (3), 1134–1141. https://doi.org/10.1021/cm902425k

[3] Nicollet C., Flura A., Vibhu V., Rougier A., Bassat J.M., Grenier J.C. (2016). An innovative efficient oxygen electrode for SOFC: Pr6O11 infiltrated into Gd-doped ceria backbone. International Journal of Hydrogen Energy,41 (34), 15538-15544, https://doi.org/10.1016/j.ijhydene.2016.04.024

[4] Thangadurai V., Huggins R.A., Weppner W. (2001). Mixed ionic-electronic conductivity in phases in the praseodymium oxide system. J. Solid State Electrochem., 5 (2001), 531-537.
https://doi.org/10.1007/s100080000187

[5] Hyde B. G., Bevan D. J. M., Eyring L. (1966). On the Praseodymium+Oxygen System. Philosophical Transactions of the Royal Society of London. Series A, Mathematical and Physical Sciences, 259 (1106), 583–614. http://www.jstor.org/stable/73275

[6] Jiang Z., Xia C., Chen F. (2010). Nano-structured composite cathodes for intermediate-temperature solid oxide fuel cells via an infiltration/impregnation technique. Electrochimica Acta, 55 (11), 3595–3605. https://doi.org/10.1016/j.electacta.2010.02.019

[7] Namgung Y., Kumar A., Hong J., Kim I-H., Song S-J. (2021). Unraveling the problem associated with multi-cation oxide formation using urea-based infiltration techniques for SOFC application. Journal of Alloys and Compounds, 852, 157037. https://doi.org/10.1016/j.jallcom.2020.157037

[8] Savinkina E.V., Karavaev I.A., Grigoriev M. S. (2020). Crystal structures of praseodymium nitrate complexes with urea, precursors for solution combustion synthesis of nanoscale praseodymium oxides, Polyhedron, 192, 114875. https://doi.org/10.1016/j.poly.2020.114875

Keywords: EFCF2024, Solid Oxide Technologies, SOC, Fuel Cells, SOFC, SOEC, Oxygen electrode, Air electrode, Pr_6O_{11}, Urea, Infiltration, Surface decoration